Designing Low-Thrust Trajectories for a SmallSat Mission to Sun-Earth L5*

Ian Elliott,† Christopher Sullivan Jr.,* and Natasha Bosanac‡
University of Colorado Boulder, Boulder, CO 80303

Jeffrey R. Stuart § and Farah Alibay ¶
Jet Propulsion Laboratory, California Institute of Technology, Pasadena, CA 91109

A small satellite deployed to Sun-Earth L_5 could serve as a low-cost platform to observe solar phenomena. However, the small satellite form factor introduces significant challenges into the trajectory design process via limited thrusting capabilities, power and operational constraints, and fixed deployment conditions. To address these challenges, a strategy employing dynamical systems theory is used to design a trajectory for a low-thrust enabled small satellite to reach the Sun-Earth L_5 region. This procedure is demonstrated for a small satellite that launches as a secondary payload with a larger spacecraft that is destined for a Sun-Earth L_2 halo orbit. Low-thrust trajectories, delivering the spacecraft from a deployment condition in the Earth vicinity to an L_5 science orbit, are produced for both an ESPA-class SmallSat and a 6U CubeSat. These solutions demonstrate the value of a dynamical systems approach to trajectory design, while also supporting the potential for small satellite missions to perform targeted heliophysics-based scientific observations well beyond low Earth orbit.

I. Introduction

The vicinity of the Sun-Earth (SE) L_5 equilibrium point, located at the vertex of an equilateral triangle formed with the Sun and the Earth, has been of much interest in the heliophysics and space weather communities as a candidate region for locating a space-based platform for solar observations and monitoring. At SE L_5, a spacecraft could observe coronal mass ejections from a perspective that is currently unavailable [1]. Furthermore, an observing platform at SE L_5 may potentially enable an improved understanding of the three-dimensional structure of coronal mass ejections when used in conjunction with space-based assets in the vicinity of the Earth. Additionally, due to the rotation of the Sun, early warning of solar storms is possible from SE L_5 [2, 3]. This equilibrium point has previously been visited by the

*An earlier version of this paper was presented as Paper No. AAS 19-266 at the 29th AAS/AIAA Space Flight Mechanics Meeting in Ka'anapali, Hawaii, January 13-17, 2019.

†Graduate Research Assistant, Colorado Center for Astrodynamics Research, Smead Department of Aerospace Engineering Sciences, 429 UCB, University of Colorado Boulder, Boulder, CO 80303, AIAA Student Member.

‡Assistant Professor, Colorado Center for Astrodynamics Research, Smead Department of Aerospace Engineering Sciences, 429 UCB, University of Colorado Boulder, Boulder, CO 80303, AIAA Member.

§Technologist, Jet Propulsion Laboratory, California Institute of Technology, Pasadena, CA 91109, AIAA Member.

¶Systems Engineer, Jet Propulsion Laboratory, California Institute of Technology, Pasadena, CA 91109, AIAA Member.

Solar TErrestrial RElations Observatory B (STEREO-B) spacecraft. Although STEREO-B did not maintain bounded motion in the vicinity of SE L_5, observations taken as the spacecraft drifted through the region have indicated the potential for advancement in fundamental heliophysics science and space weather monitoring via a spacecraft located near SE L_5 over a longer time interval.[4–6]. These findings have inspired a variety of mission concepts for spacecraft to revisit this region and has motivated an exploration of the associated trajectory design space.

With the increasing availability of rideshare opportunities and the recent demonstration of CubeSats operating in deep space during the Mars Cube One (MarCO) mission [7], small satellites may soon have the potential to visit SE L_5 to achieve heliophysics-based science objectives. While small satellites have emerged as a low-cost option for performing on-orbit science, their form factor introduces several challenges into the trajectory design process. These challenges include constrained deployment conditions due to their status as a secondary payload as well as limited operational capabilities such as available thrust, propellant mass, and power generation [8]. In this paper, two spacecraft models are considered, representing the upper and lower capabilities of the small satellite form factor [9]. At the lower capability end of the small satellite class is a 6U CubeSat equipped with a low-thrust electrospray engine, which is currently in development as a modular, commercial off-the-shelf propulsion system [10]. An ESPA-class SmallSat with a Hall-effect thruster is considered as the current high-performance upper bound of the small satellite class [9]. For spacecraft with form factors between these two extremes, the properties of representative propulsion systems and driving constraints influence the characteristics and existence of trajectories to SE L_5 from a fixed deployment condition.

Previous researchers have developed procedures for designing trajectories in multi-body systems, particularly those that connect the close proximity of the Earth to the SE L_5 region using a variety of spacecraft propulsion systems. For instance, Lo et al. [11] as well as Llanos et al. [12] explore the construction and properties of solutions that deliver a spacecraft from low Earth orbit to a short period orbit near L_5 via impulsive maneuvers. Each of these analyses begins with a trajectory constructed in the Circular Restricted Three-Body Problem (CR3BP) to predict the characteristics of similar solutions in more complex ephemeris models. The result is a trajectory design space that is complex, often necessitating trades between transfer time, launch opportunities, and propulsion requirements. However, impulsive maneuvers are not the only mechanisms for achieving transfers into an orbit near L_5 and, when they are large, may be infeasible for a small satellite to implement. In fact, low-thrust propulsion systems and solar sails supply an additional acceleration that, when activated over long time intervals, may also enable a spacecraft to reach L_5 from the Earth vicinity with similar flight times [13, 14]. Yet, the use of finite duration maneuvers in combination with the chaotic dynamics in the Sun-Earth gravitational environment introduces additional complexity into the trajectory design process. In addressing these challenges, researchers including Farrés, et al. [15] and Sood and Howell [16] have studied the underlying dynamical structures governing the motion of a solar sail in a multi-body system to reveal insights into the solution space. Using this knowledge of natural and perturbed fundamental solutions, dynamical systems techniques have enabled the design of complex trajectories within multi-body systems [15–18]. However, these approaches must be extended when designing trajectories for small satellites subject to a variety of operational and hardware constraints [19]. Furthermore, the limited trajectory design support available to low cost missions necessitates that these approaches enable rapid recovery of a reasonable point solution without a prohibitive analysis or computational burden.

In this paper, dynamical systems techniques are used to design complex, low-thrust-enabled trajectories that also satisfy several constraints associated with small satellite missions [20]. First, the dynamics of a spacecraft within the Sun-Earth system are approximated using the CR3BP. In this autonomous model, fundamental natural dynamical structures exist, including equilibrium points, periodic orbits, quasi-periodic orbits, and manifolds. Analysis of these natural motions offers insight into the design of an initial guess for an efficient low-thrust trajectory that begins at a fixed deployment condition [19]. In particular, constants of motion and their associated bounds on feasible motion guide the design of itineraries and heuristic thrusting strategies. Then, arcs along natural structures are assembled and connected via low-thrust segments to form an initial guess for an end-to-end trajectory [19]. In the Sun-Earth system, these structures tend to reflect the geometry of motions that exist in high fidelity ephemeris models [21]. To effectively transition this discontinuous initial guess, assembled in the CR3BP, to a point mass ephemeris model of the Sun-Earth-Moon system, a multiple shooting corrections strategy is used. This general procedure is outlined in this paper, improving upon previous work by Bosanac et al. [9]. This approach is then applied to the design of a low-thrust trajectory for a SmallSat and CubeSat to each visit Sun-Earth L_5 from a fixed deployment condition in the vicinity of Earth. The presented results demonstrate the use of dynamical systems theory to design low-thrust trajectories with limited required propulsive effort and subject to a variety of mission constraints. The existence of these solutions supports the potential for using small satellites to perform targeted scientific observations for heliophysics from locations well beyond low Earth orbit. Furthermore, the presented approach may be useful in subsequent analyses to seed an initial guess for optimization; support rapid redesign as the spacecraft or mission parameters evolve; or explore the design space as the trajectory segments and maneuvers are modified [22].

II. Spacecraft Models

To design a low-thrust-enabled trajectory, the baseline spacecraft configurations and associated propulsion systems must first be defined. To capture a variety of characteristics for small satellites, two spacecraft models are leveraged based on current technological capabilities [9]. First, an ESPA-class SmallSat with a Hall-effect thruster represents small satellites with a high available thrust and specific impulse I_{sp}[23]. Then, a 6U CubeSat with an electrospray engine is used to represent smaller spacecraft with a lower available thrust and specific impulse [24]. Table 1 summarizes both spacecraft models and the associated parameters used in this study, using quantities first presented by Bosanac et al. [9]. While the two spacecraft configurations are different, the ratios of the thrust to the initial wet mass are on a similar order of magnitude. Thus, a similar design process is used to design low-thrust trajectories for these two spacecraft.

Table 1 Characteristics of baseline spacecraft configurations

Parameter	ESPA SmallSat [23]	6U CubeSat [24]
Initial Wet Mass, kg	180	14
Available Thrust, mN	13	0.4
Specific Impulse, s	1375	1250
Available Propulsion Power, W	200	10

III. Dynamical Models

Models of increasing fidelity are leveraged in a dynamical systems approach to designing a complex path for a small satellite in a multi-body system, subject to a variety of constraints. Initially employing the lower-fidelity CR3BP, where possible, guides the trajectory design process via a rapid analysis of natural dynamical structures. Arcs selected from these structures to satisfy the mission constraints are then assembled and combined with low-thrust segments to create an initial guess with a desired geometry. This discontinuous guess is then transitioned to a higher-fidelity point mass ephemeris model and corrected for continuity. This approach of gradually increasing the model fidelity reduces the computational complexity and effort required to identify feasible yet constrained transfers [20, 21, 25].

A. Circular Restricted Three-Body Problem

In the multi-body gravitational environment of the Sun-Earth system, the CR3BP offers a useful approximation of the nonlinear and chaotic dynamics of an assumed massless particle P_3. The CR3BP approximates the path of two primary bodies, the Sun P_1 and the Earth P_2, via circular orbits about their mutual barycenter [26]. A Sun-Earth rotating frame $\hat{x}\hat{y}\hat{z}$ is defined to rotate with these primary bodies: P_1 and P_2 are fixed along the horizontal $\hat{x}$ axis, the $\hat{z}$ axis is then defined in the direction of the angular velocity of the system and the $\hat{y}$ axis completes the right-handed coordinate frame. Quantities in the CR3BP are then nondimensionalized. Length quantities are normalized by the distance between the primary bodies, and time quantities are nondimensionalized to produce a mean motion of P_1 and P_2 that is equal to unity. Finally, mass is nondimensionalized by the total mass of the primaries. Then, the mass ratio μ of the system is defined as $\mu = m_2/(m_1 + m_2)$ where m_1 and m_2 are the masses of the primary bodies and $m_2 \leq m_1$ [17]; in the Sun-Earth system, $\mu \approx 3.0035 \times 10^{-6}$. With these definitions, the nondimensional state vector $\boldsymbol{x} = [x, y, z, \dot{x}, \dot{y}, \dot{z}]^T$ describes the state of P_3 in the rotating frame relative to the barycenter of the system. Then, the nondimensional equations of natural motion in the rotating frame are written as:

$$\ddot{x} = 2\dot{y} + \frac{\partial U^*}{\partial x}, \qquad \ddot{y} = -2\dot{x} + \frac{\partial U^*}{\partial y}, \qquad \ddot{z} = \frac{\partial U^*}{\partial z} \tag{1}$$

where U^* is the pseudo-potential function, defined as $U^* = (1/2)(x^2 + y^2) + (1 - \mu)/r_1 + \mu/r_2$. The distances $r_1 = \sqrt{(x + \mu)^2 + y^2 + z^2}$ and $r_2 = \sqrt{(x - 1 + \mu)^2 + y^2 + z^2}$ are the distances to P_3 from P_1 and P_2, respectively [27].

The Jacobi constant C_J is a energy-like integral of motion that exists in the CR3BP and in the rotating frame. This quantity is defined as $C_J = 2U^* - (\dot{x}^2 + \dot{y}^2 + \dot{z}^2)$ and is constant along a natural trajectory. Using this definition, a low value of the Jacobi constant is analogous to a higher energy for the spacecraft as it moves within the Sun-Earth system. Although the Jacobi constant is only conserved in the CR3BP, and not in any higher fidelity models, it is valuable in preliminary trajectory design activities.

B. Point Mass Ephemeris Model

A point mass ephemeris model is constructed using information about celestial bodies available through NASA's SPICE toolkit to produce a high-fidelity model of the dynamics in the Sun-Earth environment [28]. The forces assumed to act on the spacecraft in this dynamical model include the point mass gravitational effects of the Sun, Earth, and Moon. To formulate the equations of motion, the mass of the spacecraft is considered to have a negligible gravitational effect on the primary bodies and the ephemerides of the Sun, Earth, and Moon are extracted from SPICE. Next, dimensional parameters are normalized using the same characteristic quantities as in the CR3BP [19]. Then, the nondimensional spacecraft state vector $\boldsymbol{X} = [X, Y, Z, \dot{X}, \dot{Y}, \dot{Z}]^T$ is defined in an Earth-centered inertial coordinate system. Using these definitions, the natural, nondimensional equations of motion for the spacecraft in the inertial frame are written as:

$$\ddot{\boldsymbol{R}}_{E,sc} = G\left[-m_E\left(\frac{\boldsymbol{R}_{E,sc}}{R_{E,sc}^3}\right) + m_S\left(\frac{\boldsymbol{R}_{sc,S}}{R_{sc,S}^3} - \frac{\boldsymbol{R}_{E,S}}{R_{E,S}^3}\right) + m_M\left(\frac{\boldsymbol{R}_{sc,M}}{R_{sc,M}^3} - \frac{\boldsymbol{R}_{E,M}}{R_{E,M}^3}\right)\right] \tag{2}$$

where G is the nondimensionalized gravitational constant and m corresponds to the mass of each celestial body [19, 25]. The subscript sc indicates the spacecraft, E the Earth, S the Sun, and M the Moon. Then, the relative vector $\boldsymbol{R}_{i,j}$ locates body i with respect to body j. Additional external perturbations are not reflected in this model.

C. Low-Thrust-Enabled Dynamical Models

To accurately model the maneuvers performed by a small satellite, the additional acceleration due to a low-thrust propulsion system is incorporated into the equations of motion for both the CR3BP and the point mass ephemeris model. First, to incorporate the effects of a low-thrust engine into either dynamical model, the state vector is augmented by the mass of the spacecraft, m_{sc}, which is expressed in units of kilograms. Then, a first-order scalar differential equation reflecting the mass loss due to propellant usage is written using the mass flow rate equation. Assuming a constant thrust T and a constant I_{sp}, the dimensional rate of change of the mass of the spacecraft $\dot{m}_{sc}$ is expressed as:

$$\dot{m}_{sc} = -\frac{T}{I_{sp}\ g_0} \tag{3}$$

where g_0 is the gravitational acceleration measured at the surface of the Earth, $g_0 \approx 9.81$ m/s^2. During numerical integration, this first-order equation is normalized only by the characteristic time quantity. Then, thrust direction unit vectors are originally defined in a velocity, normal, co-normal (VNC) frame with respect to the Earth as measured in the inertial frame $\hat{X}\hat{Y}\hat{Z}$ to enable the use of heuristics in maneuver planning [20]. This thrust direction is transformed into the rotating frame and added to Eq. (1) to create the following equations of motion for the low-thrust-enabled CR3BP:

$$\ddot{x} = 2\dot{y} + \frac{\partial U^*}{\partial x} + \frac{T^*}{m_{sc}} u_x, \qquad \ddot{y} = -2\dot{x} + \frac{\partial U^*}{\partial y} + \frac{T^*}{m_{sc}} u_y, \qquad \ddot{z} = \frac{\partial U^*}{\partial z} + \frac{T^*}{m_{sc}} u_z \tag{4}$$

where (u_x, u_y, u_z) are the components of the thrust direction unit vector in the rotating frame and T^* is the thrust magnitude that is normalized only by the length and time characteristic quantities. Similarly, in the point mass ephemeris model, the thrust direction unit vector is transformed into the Earth-centered inertial frame to produce the $\hat{U}$ unit vector. Then, the acceleration due to the low-thrust engine is used to modify the point mass ephemeris model from Eq. (2) to produce the following second-order vector differential equation:

$$\ddot{\boldsymbol{R}}_{E,sc} = G\left[-m_E\left(\frac{\boldsymbol{R}_{E,sc}}{R^3_{E,sc}}\right) + m_S\left(\frac{\boldsymbol{R}_{sc,S}}{R^3_{sc,S}} - \frac{\boldsymbol{R}_{E,S}}{R^3_{E,S}}\right) + m_M\left(\frac{\boldsymbol{R}_{sc,M}}{R^3_{sc,M}} - \frac{\boldsymbol{R}_{E,M}}{R^3_{E,M}}\right)\right] + \frac{T^*}{m_{sc}}\hat{U} \tag{5}$$

Modifying the CR3BP and point mass ephemeris model with the additional acceleration associated with a low-thrust engine enables the efficient generation of low-thrust arcs and, then, incorporation into the trajectory design process.

IV. Insights from Dynamical Systems Theory

A. Natural Dynamical Structures

The CR3BP admits a large variety of fundamental solutions that are useful in analyzing and predicting the solution space within a higher-fidelity model of the Sun-Earth system. Specifically, equilibrium points, periodic orbit families, and invariant manifolds tend to guide the flow within the Sun-Earth system modeled by the CR3BP and are approximately retained in a point mass ephemeris model. Five equilibrium points exist, representing constant solutions in the rotating frame, including the collinear equilibrium points (L_1, L_2, L_3) and the triangular equilibrium points (L_4, L_5). The collinear equilibrium points lie along the $\hat{x}$ axis of the rotating frame while the triangular equilibrium points form an equilateral triangle with the primary bodies in the xy-plane of the rotating frame [26]. At a system mass ratio equal to that of the Sun-Earth system, the collinear equilibrium points are unstable equilibria, admitting stable and unstable manifolds that connect the flow between various regions of the system [17]. The triangular equilibrium points, however, are stable in this system [17, 29]. Further insight into the solution space is revealed by studying the nearby periodic orbits, quasi-periodic orbits, and manifolds as well as the accessibility of the configuration space.

For a fixed value of the Jacobi constant, the motion of the spacecraft is constrained within the configuration space. The boundary between reachable and forbidden regions of the configuration space are zero-velocity surfaces; their intersection with the xy plane produces zero-velocity curves (ZVCs) [17]. The ZVCs supply valuable insight

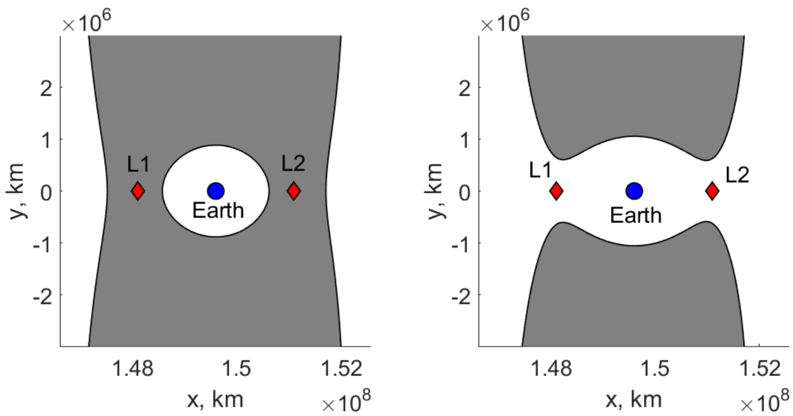

(a) $C_J(L_2) < C_J(L_1) < C_J$ **(b)** $C_J < C_J(L_2) < C_J(L_1)$

Fig. 1 Zero velocity curves in the Sun-Earth CR3BP.

into whether the energy of a spacecraft must be increased or decreased to modify the accessible regions within the configuration space. Figure 1 displays the ZVCs for two distinct values of the Jacobi constant in a Sun-Earth rotating frame using dimensional coordinates. In this figure, gray shaded regions correspond to regions of forbidden motion where a spacecraft cannot be located for a given value of the Jacobi constant in the CR3BP and white regions in the figure represent locations in the xy plane where a spacecraft may travel naturally. Then, equilibrium points are displayed as red diamonds. As the Jacobi constant is decreased below the values of the Jacobi constant corresponding to L_1 and L_2, the ZVCs define "gateways" around the equilibrium points. For instance, in the Sun-Earth CR3BP, for a spacecraft to depart the vicinity of the Earth, it must pass through either the L_1 or L_2 gateway [17]. In Fig. 1(a), the ZVCs are computed at a value of the Jacobi constant higher than the Jacobi constant value corresponding to both L_1 and L_2. For this case, both the L_1 and L_2 gateways are closed, preventing the spacecraft from departing the Earth vicinity in the CR3BP. In fact, a maneuver that increases the energy of the spacecraft would be required to lower the Jacobi constant and open the gateways to resemble Fig. 1(b). In Fig. 1(b), the spacecraft may depart from the Earth vicinity via the L_1 and L_2 gateways. Although these boundaries are only precisely defined and fixed for a single value of the Jacobi constant in the CR3BP, the ZVCs offer an approximation of the bounds on motion in the higher fidelity ephemeris model. Thus, a preliminary analysis using the zero velocity curves and surfaces supplies useful insight into a variety of preliminary trajectory design activities such as itinerary design and the heuristics for initial maneuver planning.

In the trajectory design process leveraged in this analysis, families of periodic orbits in the vicinity of the equilibrium points are valuable for mission orbit selection and initial guess construction. Many members of the Lyapunov, halo, and vertical periodic orbit families associated with L_1, L_2, and L_3 admit invariant manifolds that capture the flow of natural motion towards or away from the orbit [18]. These stable and unstable manifolds govern the existence and characteristics of natural and low-cost transfers within the system. An example of the stable and unstable manifolds emanating from L_1 and L_2 Lyapunov orbits at the same value of the Jacobi constant in the Sun-Earth system is illustrated in Fig. 2,

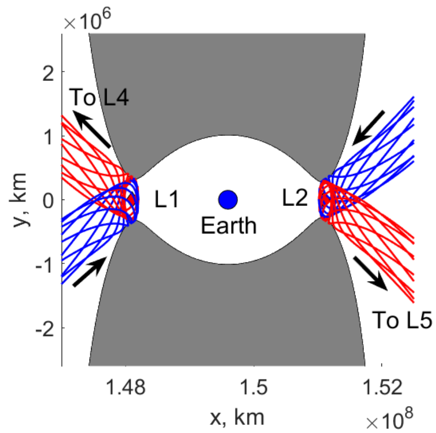

Fig. 2 Stable (blue) and unstable (red) manifolds associated with L_1 and L_2 Lyapunov orbits at the same value of C_J in the Sun-Earth CR3BP.

with a focus on the natural flow into and away from the vicinity of Earth. The stable manifolds are plotted in blue, flowing towards each associated Lyapunov orbit. Similarly, the unstable manifolds, displayed in red, flow away from each Lyapunov orbit. Examining the unstable manifolds emanating from a periodic orbit near L_2 reveals that a trajectory along an associated unstable manifold will naturally tend towards the vicinity of L_5 [15]. Similarly, trajectories that lie along an unstable manifold of an L_1 orbit naturally approach the L_4 region. However, these trajectories possess a significantly higher value of the Jacobi constant than a small periodic orbit near L_5. In this case, a maneuver may be employed to decrease the Jacobi constant and adjust the path to insert into a bounded trajectory near L_5. Thus, a transfer from the Earth vicinity to an orbit encircling SE L_5 may be constructed using the natural flow through the SE L_2 gateway, the unstable manifolds associated with periodic orbits in the SE L_2 neighborhood and low-thrust maneuvers.

The triangular equilibrium points, L_4 and L_5, admit a variety of stable periodic orbits. These periodic orbit families include short period, long period, and vertical orbits and are approximately retained in higher-fidelity models [30]. Large long period orbits exhibit extreme fluctuation in the distance from the Earth and the angle from the Sun-Earth line, which may introduce unnecessary operational challenges, such as those associated with a changing viewing angle of the Sun. From a trajectory design standpoint, vertical orbits that exist near L_5 exhibit a large out-of-plane motion at a high energy level and, therefore, may be challenging to reach from a deployment condition that lies close to the ecliptic plane or possesses a lower energy. Short period orbits near L_5, however, tend to possess a period of approximately one year in the Sun-Earth system. Several of these periodic orbits along the L_5 short period family are displayed in Fig. 3 in the SE rotating frame using dimensional coordinates. The location of the Sun and Earth are depicted with yellow and blue markers, respectively. The selected short period orbits are plotted in blue and exhibit clockwise motion around L_5, which is depicted as a red diamond. Along this short period orbit family, as the orbits emanate away from the equilibrium point, the Jacobi constant decreases from the bounding value of the Jacobi constant associated with L_5, i.e.,

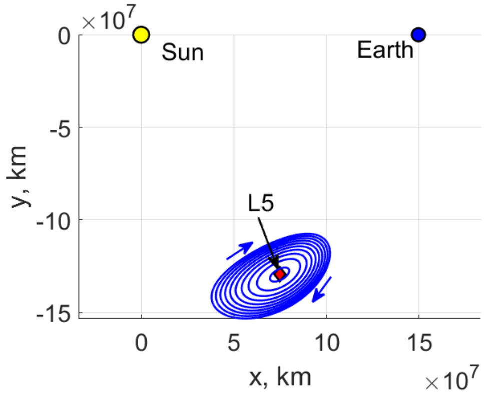

Fig. 3 Periodic orbits sampled along the SE L_5 short period family.

approximately 2.9996; the Jacobi constant of the largest short period orbit plotted in this figure is 2.9861. Furthermore, each member of the L_5 short period orbit family displayed in Fig. 3 is stable; thus, no stable or unstable manifolds exist in the CR3BP to generate a natural approach arc [29]. Stable periodic orbits serve as suitable candidates for a science orbit as the trajectory tends to remain in the vicinity of the original orbit when transitioned to an ephemeris model.

B. Poincaré Mapping

Poincaré maps enable visualization of a complex solution space by capturing the intersection of many trajectories with a selected hyperplane, e.g., defined as a higher-dimensional plane at a fixed value of a coordinate in the rotating frame [31]. Representation of these intersections on a lower-dimensional map supports the selection of arcs with favorable characteristics, such as desired flight times or Jacobi constant, for use during initial guess construction [20]. Poincaré maps are also useful for comparing the arcs from within two segments of an itinerary to construct an initial guess for a continuous trajectory. Specifically, selecting arcs that intersect the hyperplane with similar states enables construction of an initial guess with small discontinuities between segments of the end-to-end trajectory to potentially bias the corrections algorithm towards a nearby, smooth solution with a desired geometry or set of characteristics.

V. Trajectory Corrections in an Ephemeris Model

To recover a continuous trajectory from a discontinuous initial guess in a low-thrust-enabled point mass ephemeris model, a multiple shooting corrections algorithm is employed [25]. Implementing a multiple shooting algorithm begins by discretizing an initial guess for a trajectory into a sequence of N arcs. A free variable vector is then constructed to describe each arc along the trajectory. Next, a constraint vector is formed to assess continuity between neighboring arcs and the satisfaction of any additional constraints. Newton's method is then used to update the free variable vector and, therefore, simultaneously adjust each arc in an iterative manner until the constraint vector possesses a magnitude of zero to within a suitable tolerance [19]. This multiple shooting approach, relying on discretizing the path into multiple arcs, significantly reduces the sensitivity of the corrections problem while enabling the connection of natural coasting arcs and low-thrust segments. While this multiple shooting algorithm does not produce a solution that minimizes an objective function, it enables the recovery of a continuous trajectory that retains the structure of a nearby initial guess. In subsequent analyses, these solutions may be input to an optimization algorithm or transitioned to higher-fidelity models.

A free variable vector $\boldsymbol{V}$ is constructed to reflect the variables describing each arc along the solution. This free variable vector is formed by combining the individual vectors $\boldsymbol{V}_i$ describing each arc for $i = 1, \ldots, N$. If the i-th arc corresponds to a natural solution, $\boldsymbol{V}_i$ is written as:

$$\boldsymbol{V}_i = \begin{bmatrix} \boldsymbol{X}_{i,0}^T & m_{i,0} & T_i & \Delta t_i & \beta_i \end{bmatrix} \tag{6}$$

where $\boldsymbol{X}_{i,0}$ is the nondimensional state vector of the spacecraft at the beginning of the arc in the Earth-centered inertial frame, $m_{i,0}$ is the corresponding mass of the spacecraft in kg, T_i is the nondimensional time at the beginning of the arc measured from an initial epoch at the first node and Δt_i is the nondimensional integration time along the arc [25]. Then, β_i is a slack variable used to ensure a positive integration time along the i-th arc. For the N-th node, the β_i and Δt_i variables are excluded from $\boldsymbol{V}_i$. If the i-th arc is generated with a low-thrust maneuver, the $\boldsymbol{V}_i$ vector is defined as:

$$\boldsymbol{V}_i = \begin{bmatrix} \boldsymbol{X}_{i,0}^T & m_{i,0} & T_i & \Delta t_i & \beta_i & \hat{u}_i^T \end{bmatrix} \tag{7}$$

where the thrust direction, $\hat{u}_i$, is constant along the entire arc in the VNC frame with respect to the Earth. Maintaining a constant thrust direction in this frame is considered a reasonable assumption in this preliminary analysis for short maneuvers applied near the Earth and longer low-thrust-enabled arcs far from the Earth; in higher-fidelity analyses, operational constraints on the thrust direction may be incorporated into the corrections process. During initial guess construction, a vector of binary elements is defined to reflect whether the low-thrust engine is activated over each arc and to select the correct form of $\boldsymbol{V}_i$ to include in the free variable vector [19]. Although this vector is held constant throughout each iteration of the corrections process, low-thrust arcs may be essentially removed as the integration time tends towards zero. The complete free variable vector $\boldsymbol{V}$ is then assembled as $\boldsymbol{V} = [\boldsymbol{V}_1, \boldsymbol{V}_2, \boldsymbol{V}_3, \ldots, \boldsymbol{V}_N]^T$. If there are N_c coast arcs, N_l low-thrust segments and one final node, the dimension of $\boldsymbol{V}$ is $(10N_c + 13N_l + 8) \times 1$.

The constraint vector $\boldsymbol{F}$ is constructed to enforce continuity between neighboring arcs, a positive integration time along each arc and to fix the initial conditions. Individual components $\boldsymbol{F}_i$ of the constraint vector capture the discontinuity between the end of the i-th arc and the beginning of the $(i+1)$-th arc for $i = 1, \ldots, (N-1)$. If the i-th arc corresponds to natural motion, the vector $\boldsymbol{F}_i$ is written as:

$$\boldsymbol{F}_i = \begin{bmatrix} (\boldsymbol{X}_{i,f} - \boldsymbol{X}_{i+1,0})^T & (m_{i,f} - m_{i+1,0}) & (T_i + \Delta t_i - T_{i+1}) & (\Delta t_i - \beta_i^2) \end{bmatrix} \tag{8}$$

where $\boldsymbol{X}_{i,f}$ is the state at the end of the i-th arc [19]. The final element of this vector constrains the integration time to retain a positive value; the slack variable β_i is used to write this requirement as an equality constraint. When constraining a finite burn to possess at least a minimum duration, it is useful to modify this constraint to ensure an integration time that is above a minimum threshold $\Delta t_{i,\min}$. In this case, the final constraint in $\boldsymbol{F}_i$ is straightforwardly modified to the equality constraint $\Delta t_i - \beta_i^2 - \Delta t_{i,\min} = 0$. If the low-thrust engine is activated along the i-th arc, an additional constraint is introduced: the thrust direction vector must possess a unit magnitude. This scalar constraint is concatenated to the end of $\boldsymbol{F}_i$ such that the $\boldsymbol{F}_i$ vector is written as:

$$\boldsymbol{F}_i = \begin{bmatrix} (\boldsymbol{X}_{i,f} - \boldsymbol{X}_{i+1,0})^T & (m_{i,f} - m_{i+1,0}) & (T_i + \Delta t_i - T_{i+1}) & (\Delta t_i - \beta_i^2) & (|\hat{u}_i|^2 - 1) \end{bmatrix} \tag{9}$$

An additional constraint vector $\boldsymbol{F}_d$ is employed to fix the values of the initial state, epoch and mass along the trajectory equal to the deployment conditions, such that:

$$\boldsymbol{F}_d = \begin{bmatrix} (\boldsymbol{X}_{1,0} - \boldsymbol{X}_{d,0})^T & (m_{1,0} - m_{d,0}) & (T_1 - T_d) \end{bmatrix} \tag{10}$$

where $\boldsymbol{X}_{d,0}$, $m_{d,0}$ and T_d are the initial state, mass and epoch at deployment. Then, the complete constraint vector is constructed as $\boldsymbol{F} = [\boldsymbol{F}_1, \boldsymbol{F}_2, \boldsymbol{F}_3, \ldots, \boldsymbol{F}_{N-1}, \boldsymbol{F}_d]^T$ with the correct form of $\boldsymbol{F}_i$ selected using the binary vector that encodes whether the low-thrust engine is activated along each arc. For N_c coast arcs, N_l low-thrust segments and one final node, $\boldsymbol{F}$ possesses a dimension of $(9N_c + 10N_l + 8) \times 1$.

In the multiple shooting scheme used in this paper, Newton's method is employed to perform iterative updates to the free variable vector until the norm of the constraint vector is approximately zero to within an acceptable tolerance. A Jacobian matrix is formed to reflect a linear approximation of the sensitivity of each constraint to the free variables. This matrix $\boldsymbol{DF}(\boldsymbol{V})$ is constructed using a combination of analytical expressions and approximations via forward finite differencing. The dimension of $\boldsymbol{DF}(\boldsymbol{V})$ is $(10N_c + 13N_l + 8) \times (9N_c + 10N_l + 8)$. Since the Jacobian is not a square matrix, the free variables are updated at iteration j via the minimum-norm update equation:

$$\boldsymbol{V}^{j+1} = \boldsymbol{V}^j - \boldsymbol{DF}(\boldsymbol{V}^j)^T \left[\boldsymbol{DF}(\boldsymbol{V}^j)\, \boldsymbol{DF}(\boldsymbol{V}^j)^T\right]^{-1} \boldsymbol{F}(\boldsymbol{V}^j) \tag{11}$$

These updates continue until the Euclidean norm of the complete constraint vector $\boldsymbol{F}$ equals zero, to within an appropriate tolerance, e.g., 10^{-10}, indicating recovery of a continuous trajectory that satisfies all the constraints. This multiple shooting scheme is employed to recover both a continuous trajectory and the associated thrust profile.

VI. Trajectory Design Process

In this paper, a dynamical systems approach to trajectory design is applied to a SmallSat that is assumed to ride as a secondary payload on a space telescope mission to a SE L_2 southern quasi-halo orbit with the goal of reaching the SE L_5 region. For this sample telescope mission, the launch date is assumed to occur on January 1, 2025, and the initial deployment condition for the SmallSat is 24 hours after departing a 300 km altitude, 28.5° inclination orbit. These characteristics reflect a secondary payload that is deployed from the primary spacecraft during its transfer from the Earth vicinity and well before the primary mission maneuvers to enter the science orbit. To design a low-thrust-enabled transfer from this deployment condition to the SE L_5 region, the general itinerary is discretized into three segments:

1) A departure phase from deployment in the Earth vicinity to the transfer through the SE L_2 gateway, using a combination of natural and low-thrust arcs
2) A predominantly natural transfer segment between the SE L_2 gateway and the vicinity of SE L_5
3) A low-thrust-enabled insertion into a bounded science orbit around SE L_5

From the constrained deployment condition, brief low-thrust maneuvers are leveraged to identify arcs that depart through the L_2 gateway. Natural unstable manifold structures associated with SE L_2 halo orbits are then analyzed to identify suitable initial guesses for the transfer segment between SE L_2 and SE L_5. Next, L_5 short period orbits are characterized in the Sun-Earth CR3BP to identify candidate bounded motions for the science phase of the mission. Following selection of a suitable science orbit, low-thrust approach arcs are generated backwards in time from the periodic orbit and analyzed for their potential to connect to the natural manifolds of a SE L_2 orbit. Poincaré mapping strategies are used to identify arcs within each segment that enable construction of an initial guess that possesses small discontinuities. Selected arcs are assembled along with additional low-thrust maneuvers to form an initial guess that is corrected via multiple shooting; the result is a low-thrust trajectory for the SmallSat in a point mass ephemeris model.

A. Departure from the Earth Vicinity Following Deployment

When propagated naturally in a point mass ephemeris model of the Sun, Earth, and Moon, the deployment conditions produce a trajectory that departs through the SE L_2 gateway. This trajectory is displayed in Fig. 4 in a Sun-Earth rotating frame using dimensional coordinates, measured relative to the Sun-Earth barycenter. The trajectory of the SmallSat, propagated naturally for one year, is depicted in this figure in blue and the orbit of the Moon is colored gray. The L_1 and L_2 equilibrium points are located by red diamonds, while the Earth is identified by a blue filled circle. For a deployment condition near the Earth, the point mass ephemeris model is used to generate the path of the spacecraft during this departure phase due to the influence of the gravity of the Moon and the variations in the path of the Earth from a circular reference orbit [20]. As displayed in Fig. 4, the natural path associated with the deployment condition resembles a trajectory on the stable manifold of a SE L_2 halo orbit. Furthermore, the value of the Jacobi constant along this trajectory offers valuable insight into the characteristics of the path, even in an ephemeris model where C_J is no

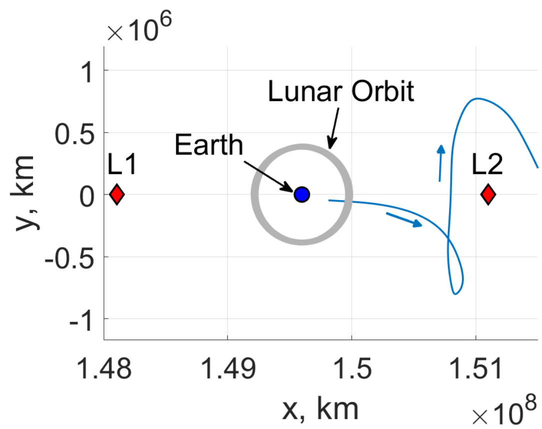

Fig. 4 Natural trajectory associated with the deployment conditions and propagated for one year in a point mass ephemeris model.

longer constant. Following deployment, the Jacobi constant along the solution displayed in Fig. 4 is approximately equal to 3.00080: lower than the Jacobi constant evaluated at SE L_2, but greater than that of SE L_5. This observation suggests that, while the spacecraft possesses enough energy to pass through the L_2 gateway, it does not possess a sufficient energy to match the Jacobi constant of L_5. Thus, to match the Jacobi constant of L_5 or insert into a small short period orbit with a similar energy to L_5, the value of C_J must eventually be decreased further: either through the variations that occur along a natural solution in an ephemeris model or via the application of long low-thrust maneuvers. However, in this phase only brief low-thrust maneuvers are applied prior to departure through the L_2 gateway to enable a connection to arcs in the next segment of the itinerary and to offer an opportunity for engine checkout activities.

To explore the array of solutions that quickly pass through the SE L_2 gateway, two low-thrust maneuvers are placed after deployment. The first maneuver is a checkout burn with a duration of two hours in the spacecraft velocity direction with respect to the Earth. This maneuver is applied after a seven day coast period post-deployment to allow time for the spacecraft to complete system initialization activities and to ensure that the engine is working properly. Following the checkout burn, another seven day coast segment is included for additional checkouts on the spacecraft. Then, a second maneuver with a duration of 72 hours is applied in a constant direction in the spacecraft's VNC frame, defined with respect to the Earth. The placement and duration of this maneuver is selected to leverage the sensitivity of the multi-body gravitational environment in the Earth vicinity to produce a sufficiently wide variety of solutions that pass through the L_2 gateway and connect to suitable arcs in the subsequent segment of the itinerary; these properties may be adjusted in subsequent analyses to enable exploration of the solution space.

Through analysis of a variety of thrust directions for the second maneuver, a set of trajectories that pass through the L_2 gateway with a desired energy and geometry are generated. Specifically, 100 distinct thrust directions are randomly sampled within the VNC frame. The characteristics of these trajectories as they pass through the gateway are summarized using a Poincaré mapping strategy [20]. A subset of these solutions is displayed in Fig. 5a, with coast arcs

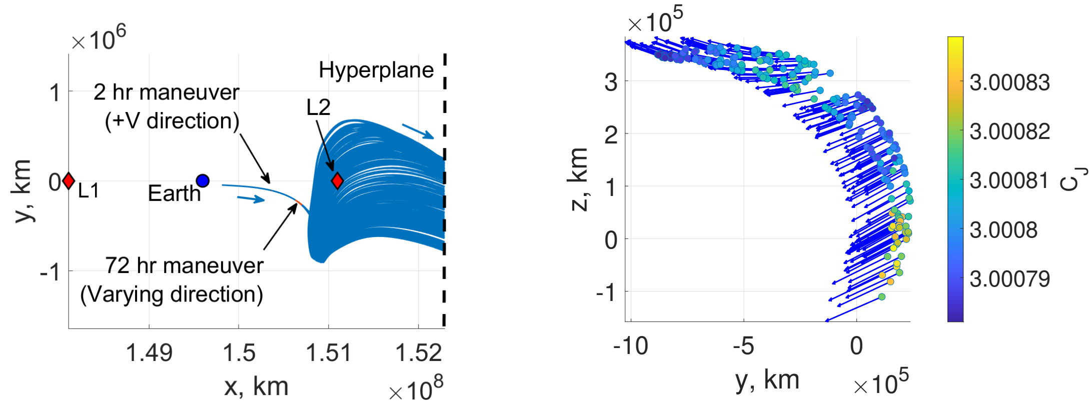

(a) Trajectories in configuration space with natural (blue) and low-thrust (red) arcs. **(b) Map summarizing low-thrust-enabled trajectories.**

Fig. 5 Low-thrust-enabled SmallSat trajectories passing through the SE L_2 gateway after deployment.

colored blue and low-thrust maneuvers displayed in red. The blue arrows indicate the general direction of motion, while the equilibrium points are displayed as red diamonds and the Earth is located by a blue filled circle. To construct a useful map, a hyperplane is defined in the rotating frame at a value of the x-coordinate slightly beyond SE L_2; this hyperplane appears in Fig. 5a as a black dashed line. By selecting a hyperplane beyond SE L_2, motion that temporarily passes through the gateway before returning to the Earth vicinity is generally excluded from the data on the map. Capturing the intersection of the set of post-deployment arcs with this hyperplane, the corresponding map is displayed in Fig. 5b. In this figure, the nondimensional y and z components of the map crossings in the Sun-Earth rotating frame are depicted on the horizontal and vertical axes, respectively. The $\dot{y}$ and $\dot{z}$ components of the state are represented by the horizontal and vertical components of the arrows attached to each map crossing while the length of each arrow is scaled to reflect the relative magnitude of the velocity across the dataset [32]. Finally, the value of the Jacobi constant at each map crossing is represented by the marker color, according to the colorbar in Fig. 5b. Analysis of this figure reveals that the Jacobi constant varies across the entire set of map crossings due to differences in the energy change resulting from low-thrust maneuvers in distinct directions as well as gravitational perturbations. Although not represented on the figure, the time of flight of each trajectory captured on the map in Fig. 5b, measured from the initial deployment condition to its intersection with the hyperplane, is approximately equal to 150 days. These observations suggest that a brief low-thrust maneuver produces a small change in the Jacobi constant while adjusting the spacecraft's departure through the L_2 gateway without significantly altering the flight time.

B. Transfer From the L_2 Gateway to L_5 Vicinity

Unstable manifolds associated with periodic orbits near L_2 tend to govern natural motion towards the vicinity of L_5; thus, these dynamical structures are leveraged in the construction of an initial guess for this transfer segment [29].

There are several L_2 orbit families with members that may possess unstable manifolds, including the Lyapunov, halo, axial, and vertical families [33]. Unstable manifolds for several periodic orbits are rapidly generated in the CR3BP and analyzed for their Jacobi constant, out-of-plane amplitude, and flight time to the L_5 vicinity. Using this approach, the L_2 halo family is selected to construct a predominantly natural transfer from the L_2 gateway to insertion into the L_5 science orbit. These particular dynamical structures possess similar out-of-plane amplitudes and values of the Jacobi constant to candidate post-deployment trajectories as they pass through the L_2 gateway. The unstable manifold structures associated with members of the halo family also possess a considerably lower time of flight to L_5 when compared to the unstable manifolds of vertical and axial orbits. As an example, several trajectories along the unstable manifold associated with a SE L_2 northern halo orbit at a Jacobi constant of 3.00080, near the value of C_J for the deployment trajectories, are depicted in a SE rotating frame in Fig. 6 using dimensional coordinates. In this figure, the blue arrows represent the general direction of the flow from the Earth vicinity towards L_5, while the primaries are located by filled circles and the SE L_5 equilibrium point is identified by a red diamond. Analysis of this figure reveals a set of trajectories that deliver a spacecraft from the L_2 gateway to the vicinity of SE L_5. However, not all trajectories along the unstable manifold provide a suitable initial guess for an end-to-end trajectory and a candidate post-deployment arc. Rather, the transfer trajectory must be selected both to minimize discontinuities between the two segments and reduce the flight time.

Poincaré mapping is used to efficiently examine the trajectories along an unstable manifold associated with a SE L_2 northern halo orbit and, then, to select a single arc for use in an initial guess. By creating a map that captures both the end of the post-deployment trajectories and the beginning of the transfer from the L_2 gateway to the L_5 vicinity, individual arcs in each phase of the trajectory are selected to reduce the associated discontinuity in the initial guess. To construct this map, a hyperplane defined in the SE rotating frame at $x = 1.018$ nondimensional units is used; this definition is consistent with the hyperplane plotted in Fig. 5b. First, trajectories along the unstable manifold of a northern L_2 halo at

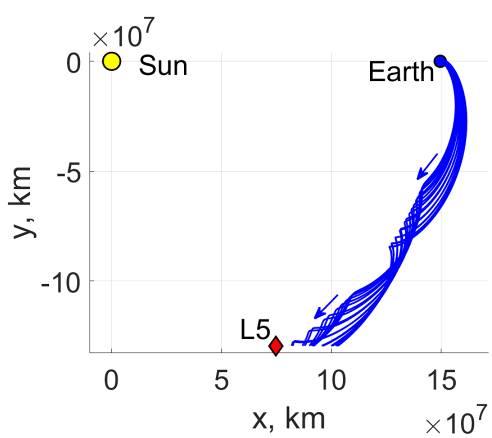

Fig. 6 Unstable manifold associated with an L_2 northern halo orbit, governing motion towards L_5.

$C_J = 3.00080$ are generated. The intersections of this manifold with the hyperplane are overlaid on the crossings of the post-deployment arc, previously displayed on the map in Fig. 5b. Then, filtering the map to only display trajectories on the unstable manifold that possess crossings close to the post-deployment arcs produces the reduced data set depicted in Fig. 7(a). This figure is constructed with the y and z components of the state vector at each map crossing displayed on the horizontal and vertical axes, respectively. The arrow associated with each crossing represents the $\dot{y}$ and $\dot{z}$ components of the state vector [32]. The color of the marker reflects the value of the Jacobi constant at each map crossing, while the color of the arrows differentiates the crossings in each segment: the post-deployment trajectories generated in the point mass ephemeris model are colored in blue, and the trajectories generated in the CR3BP to lie on the L_2 halo unstable manifold are colored in red [32]. The black box in Fig. 7(a) is expanded in Fig. 7(b) to reveal a zoomed-in view of map crossings that occur at similar locations on the hyperplane with a similar value of the Jacobi constant and velocity vectors that are closely aligned. The map in Fig. 7(b) is used to select arcs within the first two segments of the trajectory: the associated map crossings are labeled in the figure. These map crossings occur close in configuration space and possess $\dot{y}$ and $\dot{z}$ components of the state vector that are similar. In general, the arcs generated in the ephemeris model for the post-deployment segment of the mission possess a Jacobi constant that does not exactly intersect $C_J = 3.00080$, i.e., the selected Jacobi constant associated with the unstable manifold. Reducing this Jacobi constant further below $C_J = 3.00080$ would produce a larger halo orbit and the map crossings associated with the post-deployment arcs likely would not intersect the unstable manifold. Rather, the map crossings associated with post-deployment arcs would likely lie inside this structure. However, when a trajectory that lies along the unstable manifold is transitioned to a point mass ephemeris model and corrected with multiple shooting, the difference in the Jacobi constant between the arcs associated with the map crossings identified in Fig. 7(b) may be reduced to zero. Thus, the selected arcs in the post-deployment and transfer segments of the itinerary offer a suitable starting point for constructing an initial guess.

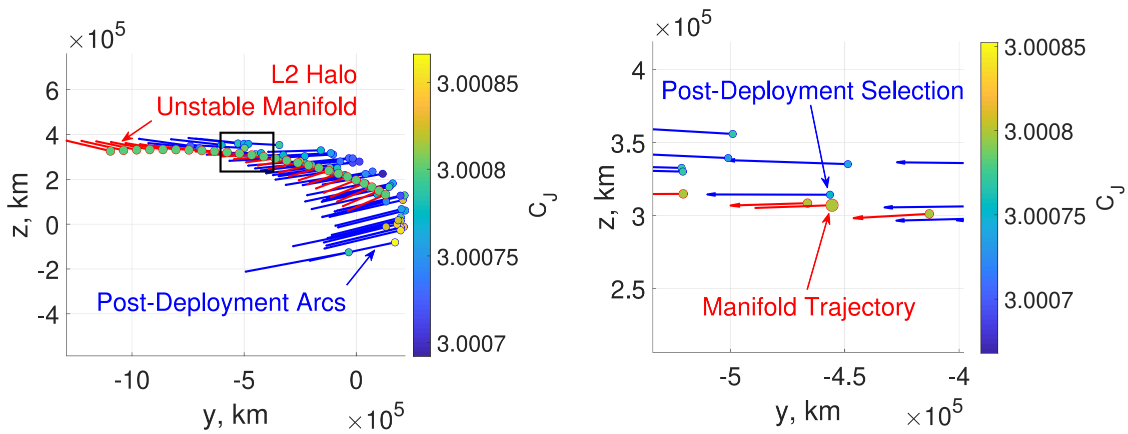

(a) Full map view

(b) Zoomed-in view of map focused on selected crossings

Fig. 7 Poincaré map summarizing crossings of the post-deployment trajectories (blue arrows) and selected SE L_2 northern halo unstable manifold (red arrows) on the same hyperplane.

C. Insertion to L_5 Science Orbit

A science orbit is designed using a periodic solution that is selected directly from the L_5 short period orbit family and generated in the CR3BP. This periodic orbit is selected to satisfy two general, but competing goals. First, the short period orbit is selected to possess a sufficiently large amplitude around L_5 to produce a variety of low-thrust-enabled arcs that insert into the orbit in forward time and connect to the transfer segment in backward time. In addition, the candidate orbit is selected to possess a higher value of the Jacobi constant occurring along the family, i.e., one that is closer to the Jacobi constant associated with the transfer segment, to implicitly reduce the thrust duration required for the long insertion maneuver. Recall that along the short period family, the Jacobi constant decreases as the periodic orbits emanate away from the L_5 equilibrium point. Balancing these two objectives, an L_5 short period orbit with a Jacobi constant of 2.995 and a period of approximately one year is used to generate a target science orbit.

To construct an initial guess for an arc that approaches the selected science orbit near L_5, a long insertion maneuver is used. The short period orbit is first discretized into several fixed points, defined in the rotating frame and in the CR3BP. For each fixed point, several low-thrust trajectories are propagated backward in time using the modified CR3BP for a variety of distinct thrust directions: 64 thrust directions are selected from an even distribution within the VNC frame. Along each trajectory, the thrust unit vector is held constant in a VNC frame with respect to the Earth for the duration of the maneuver [20]. Each trajectory is first propagated backward in time with the low-thrust engine activated for one year. Next, each trajectory is propagated backward in time with the low-thrust engine deactivated until the trajectory intersects a specified hyperplane. The spacecraft mass at all potential orbit insertion points is specified by subtracting the constant mass flow rate multiplied by a year from the spacecraft mass at the end of the transfer segment. The low-thrust propagation time is selected to ensure that the maneuver sufficiently reduces the Jacobi constant from the value of C_J associated with the selected L_2 halo orbit unstable manifold arc to the value of C_J along the selected L_5 short period orbit. This propagation time may be varied in subsequent analyses to further explore the design space. The hyperplane used to capture the generated approach arcs is defined at a fixed value of the y-coordinate in the SE rotating frame, between that of L_5 and the Earth. While there may be a variety of feasible definitions for this hyperplane, the hyperplane is constrained in this analysis to lie at a great enough distance from L_5 to capture the trajectories associated with a thrust duration of one year prior to reaching the hyperplane. The hyperplane location is also selected to lie far enough from the Earth to capture motion from the L_2 unstable manifold that is primarily in the negative y direction. Of course, using an alternative definition for the hyperplane alters the captured arcs and, influences the initial guess.

A set of low-thrust-enabled trajectories that flow into the L_5 short period orbit are generated and their intersections with the selected hyperplane are recorded. These trajectories are displayed in Fig. 8 in the SE rotating frame using dimensional coordinates, along with the final L_5 short period science orbit. In this figure, low-thrust arcs are depicted in red and natural arcs are blue, while the specified hyperplane is indicated by a black dashed line. The generated low-thrust approach arcs are visualized on a Poincaré map and compared to the intersections of the unstable manifold

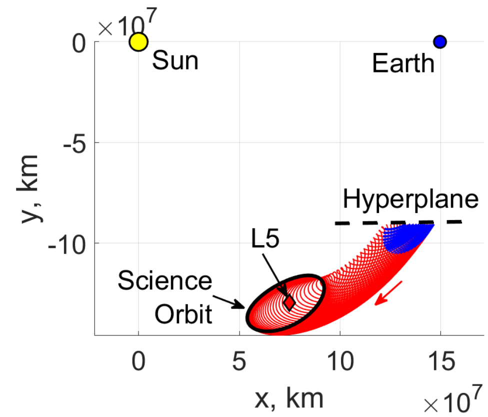

Fig. 8 Low-thrust-enabled insertion into the SE L_5 short period science orbit with natural arcs (blue) and low-thrust arcs (red).

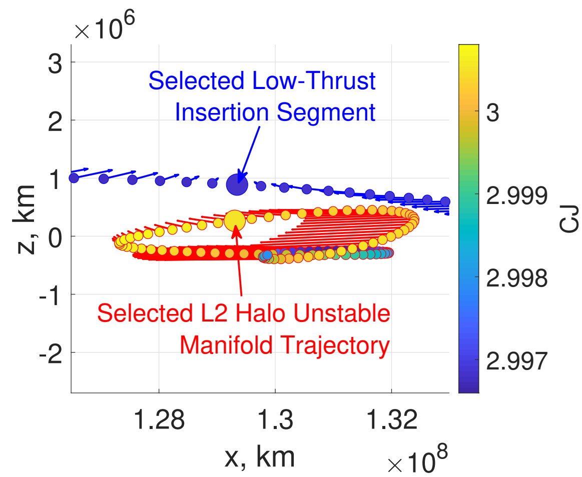

Fig. 9 Poincaré map illustrating the intersections of selected trajectories along the SE L_2 halo orbit (red) and potential low-thrust insertion trajectories (blue) with the same hyperplane.

arcs associated with the L_2 northern halo at $C_J = 3.00080$. The Poincaré map, displayed in Fig. 9, captures both the crossings of the L_2 manifold trajectories (red arrows) and low-thrust approach arcs (blue arrows) generated in the natural and modified CR3BP, respectively. This figure is constructed with the y and z components of the state vector at each map crossing displayed on the horizontal and vertical axes, respectively. The arrow associated with each crossing represents the $\dot{x}$ and $\dot{z}$ components of the state vector in the horizontal and vertical directions, respectively. Then, the map crossing associated with the transfer arc previously selected to lie along the unstable manifold of the L_2 northern halo orbit is indicated by a large circle marker and labeled. Analysis of Fig. 9 reveals that at the selected hyperplane, the set of map crossings reflecting candidate arcs in the low-thrust insertion segment consistently exhibits discontinuities in the state and Jacobi constant relative to the selected arc in the transfer segment; thus, no close intersections occur in both position and velocity. However, these discontinuities are small enough to be corrected following transition to a higher-fidelity dynamical environment and the application of the multiple shooting algorithm. Thus, this Poincaré map is used to select a low-thrust insertion arc by identifying a map crossing that possesses a similar position to the map crossing associated with the selected arc in the transfer segment as well as a reasonable time to flight; the selected map crossing is labeled in Fig. 9 and represented with a large circle marker. Once the low-thrust approach arc has been selected, several revolutions of the L_5 short period orbit are concatenated to the end of the initial guess to reflect multiple years of bounded motion during the science phase of the mission and to bias the multiple shooting algorithm to recover a solution that completes several revolutions around L_5.

D. Recovering an End-to-End SmallSat Trajectory

Once an initial guess is constructed using the individual arcs selected for each phase of the trajectory, a multiple shooting corrections algorithm is used to recover a continuous solution in the point mass ephemeris model. The arcs that are generated in the CR3BP are transformed from a rotating frame to the inertial frame, including the transfer from the L_2 gateway to the vicinity of L_5, the L_5 approach arc, and several revolutions around a short period orbit. This transformation is implemented via an origin translation, time-dependent frame rotation and dimensionalization of the states and epochs at each node using the characteristic quantities of the Sun-Earth system [34]. During this process, each node is assigned a nondimensional epoch measured relative to the deployment condition and calculated as the sum of the integration times along all previous arcs. These states at the beginning of each arc, expressed in an Earth-centered inertial coordinate system, are integrated forward in time in the point mass ephemeris model. The resulting discontinuous initial guess for an end-to-end trajectory is displayed in Fig. 10 in the SE rotating frame using dimensional coordinates. The color scheme and configuration of this figure is consistent with Fig. 5a. While the segments selected using dynamical structures from the natural and low-thrust-enabled CR3BP supply a good initial guess, there are still small discontinuities between neighboring arcs. The Jacobi constant evaluated along the entire initial guess, included in Fig. 11, supplies additional insight into the size of these discontinuities in the point mass ephemeris model. These discontinuities may influence the sensitivity of the corrections algorithm when transitioning these arcs from the natural and low-thrust-enabled CR3BP to the point mass ephemeris model, while seeking a solution that is both continuous and satisfies several additional constraints.

Due to the high sensitivity of a solution that encompasses various regions of the Sun-Earth system, the corrections process is implemented by correcting smaller segments prior to the entire end-to-end trajectory. This multi-step corrections process increases the likelihood of recovering a solution that closely resembles the initial guess. First, the post-deployment trajectory and the transfer segment are connected via the multiple shooting algorithm to produce a continuous arc in the point mass ephemeris model. During this corrections step, the initial spacecraft state, epoch, and mass are constrained to match the deployment conditions while the total flight time along these segments is allowed to vary. Then, the low-thrust approach arc and several revolutions of the science orbit are connected to produce another

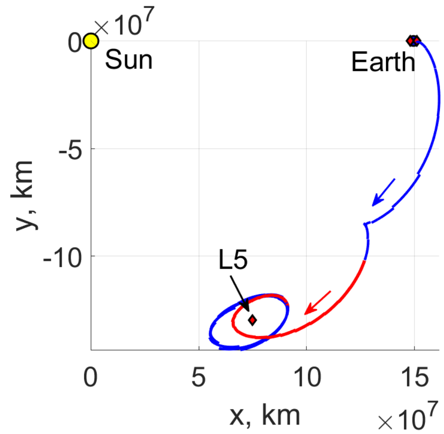

Fig. 10 Initial guess for a low-thrust trajectory for a SmallSat from deployment to an L_5 short period orbit.

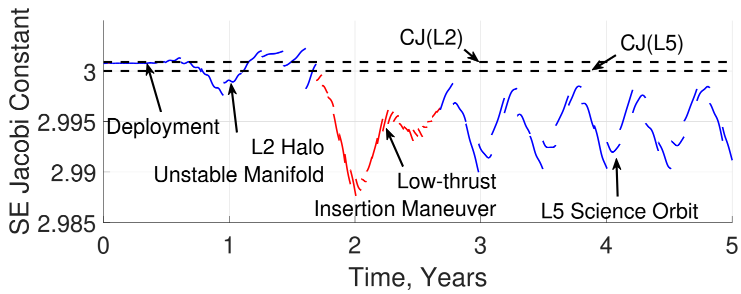

Fig. 11 Sun-Earth Jacobi constant evaluated along the initial guess for the SmallSat end-to-end trajectory.

continuous arc in the point mass ephemeris model. During this corrections step, the initial state, epoch and flight time are unconstrained. As a result of the initial guess construction process, the geometry, flight times and characteristics of the corrected arcs do not deviate significantly from the associated initial guess. Thus, significant discontinuities in state, epoch and spacecraft mass between the transfer and low-thrust approach segments are not introduced through this process. These two arcs are then corrected simultaneously to rapidly recover a nearby, continuous end-to-end trajectory.

With initial state, mass, and epoch constraints and the enforcement of continuity along the entire trajectory in the ephemeris model, the complete multiple shooting process converges to a solution that produces a constraint vector that is equal to zero to within a tolerance of 1×10^{-10}. The recovered end-to-end trajectory for the SmallSat to reach L_5 after deployment from a space telescope destined for SE L_2 is displayed in Fig. 12a in the SE rotating frame using dimensional coordinates. Natural arcs are displayed in blue and low-thrust maneuvers are colored red. A zoomed-in view of the post-deployment phase is included in Fig. 12b with a color scheme and configuration that is consistent with Fig. 12a. The time of flight for the recovered trajectory, from deployment to insertion into an L_5 science orbit, is 2 years and 211 days. Furthermore, this solution requires 30.310 kg of propellant, or 16.8% of the initial 180 kg wet mass of the spacecraft. The Jacobi constant of this trajectory, evaluated in the Sun-Earth system, is portrayed in Fig. 13 with low-thrust segments colored red and natural segments indicated via blue curves. Dotted lines locate the value

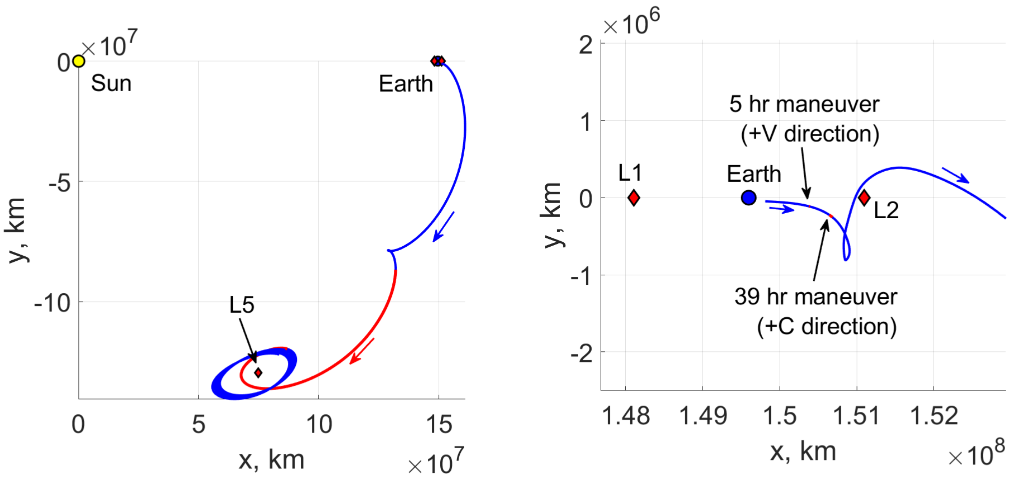

(a) End-to-end trajectory. **(b) Zoomed-in view.**

Fig. 12 Continuous low-thrust trajectory for a SmallSat from deployment to an L_5 short period orbit.

of the Jacobi constant at SE L_2 and L_5, and labels indicating the associated phase of the trajectory. In this figure, the low-thrust maneuver appears to adjust the time evolution of the value of C_J to match the values and natural oscillations that occur along a SE L_5 short period orbit in the point mass ephemeris model. Analysis of Fig. 12 and Fig. 13 reveals that the recovered solution resembles the initial guess, as expected following the use of multiple shooting. While the short period orbit is smaller in size and possesses a higher value of C_J than the associated segment of the initial guess, the characteristics of the final science orbit are not explicitly constrained. If, however, mission requirements restrict the characteristics of this science orbit, then additional constraints must be incorporated into the corrections process. Nevertheless, this result demonstrates the value of leveraging dynamical systems techniques when designing low-thrust trajectories for a SmallSat both rapidly and without a prohibitive computational or analysis burden.

In subsequent analyses, the recovered trajectory must be adjusted to increase the operational feasibility of the solution. Specifically, duty-cycling during the one year science orbit insertion burn with consideration for the communication and power generation capabilities of a SmallSat would increase the feasibility of the long duration low-thrust maneuver.

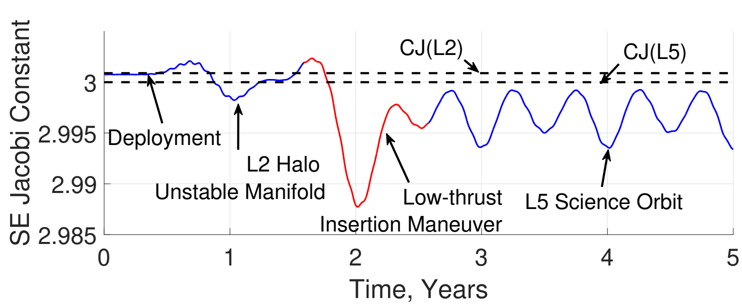

Fig. 13 Sun-Earth Jacobi constant evaluated along the corrected SmallSat end-to-end trajectory.

Additionally, if information is available on the orientation of the spacecraft's communications and solar panels, further constraints on the spacecraft's orientation during the low-thrust insertion maneuvers may be required. Nevertheless, the low-thrust trajectory in Fig. 12a supplies sufficient insight into the expected geometry and characteristics of a higher-fidelity end-to-end trajectory for the small satellite to travel to SE L_5 from a constrained deployment condition.

E. CubeSat Trajectory Design

The outlined design process is also used to recover a point solution for the 6U CubeSat from the same deployment conditions. The 6U CubeSat spacecraft model introduces additional challenges into the trajectory design process when compared to the SmallSat spacecraft model: the CubeSat has a lower ratio of the thrust to initial wet mass, thereby lowering the available acceleration from the low-thrust engine. The CubeSat's propulsion system also possesses a lower specific impulse, which results in a less efficient use of propellant mass. Despite these performance constraints, a similar trajectory design process as used with the SmallSat is used to design an end-to-end CubeSat trajectory from the vicinity of the Earth to L_5. Post-deployment, the itinerary begins with a seven day coast arc followed by a two hour checkout burn. Next, a seven day coasting segment is used for additional checkouts and is followed by a 14 day low-thrust maneuver. In the previously constructed SmallSat trajectory, this second maneuver possesses a duration of approximately 72 hours. However, in this specific example, the maneuver duration is necessarily increased to ensure that the CubeSat passes through the L_2 gateway with the desired characteristics to link to arcs in the next segment of the itinerary. Subsequent analyses may focus on reducing this maneuver duration or modifying the location. The direction of this maneuver is varied to generate a sufficient variety of candidate trajectories from post-deployment to the L_2 gateway. Then, trajectories along the unstable manifold associated with a northern L_2 halo are generated at $C_J = 3.00068$, similar to the Jacobi constant of solutions that pass through the L_2 gateway. The same SE L_5 short period orbit used in the SmallSat analysis, corresponding to a Jacobi constant of 2.995, is used to construct the initial guess for the low-thrust insertion and science orbit. Following the Poincaré mapping approach outlined in this analysis, an initial guess for the CubeSat trajectory is constructed and displayed in Fig. 14(a) in a SE rotating frame using dimensional coordinates; low-thrust arcs are colored red and natural arcs are blue. Arrows indicate direction of motion, while the primaries are located by filled circles and L_5 is identified by a red diamond. Following corrections via a multiple shooting algorithm, a nearby continuous solution is recovered and displayed in Fig. 14(b) with the same configuration and color scheme as Fig. 14(a). This point solution requires a flight time of 3.25 years, with a total maneuver time of approximately 1 year and a propellant mass of 1.33 kg, i.e., approximately 9.53% of the initial wet mass. Consistent with the SmallSat trajectory design scenario, the final orbit characteristics are not explicitly constrained during the correction process. As a result, the science orbit in the recovered trajectory possesses a smaller amplitude relative to L_5 when compared to the initial guess. However, the recovered revolutions around SE L_5 still offer a reasonable option for a science orbit.

Both the CubeSat and SmallSat trajectories share similar characteristics and geometry. The characteristics of the

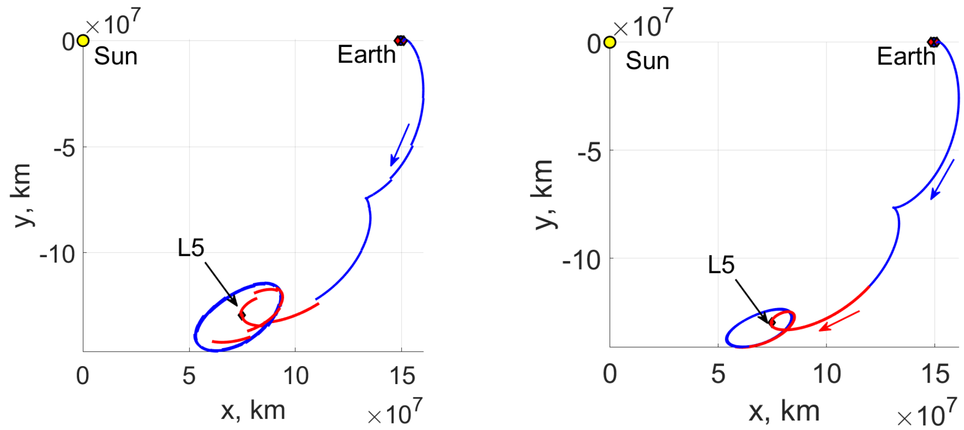

(a) Initial guess **(b) Recovered trajectory**

Fig. 14 Initial guess and recovered continuous low-thrust trajectory for a 6U CubeSat from deployment to insertion into an L_5 short period orbit.

end-to-end trajectories constructed for each of the two spacecraft models are summarized in Table 2. In this table, the time of flight is measured from deployment to the engine shutoff for the insertion maneuver into the L_5 science orbit. Notably, the time of flight for the CubeSat trajectory is longer than that of the trajectory developed for the SmallSat model. However, this difference may be attributed to the individual trajectories selected along the L_2 halo unstable manifolds during initial guess construction. Further analysis into the relationship between the application of additional finite burns may also be used to reduce the flight time for the CubeSat. However, this example demonstrates the application of the outlined trajectory design approach to different small satellite form factors and performance capabilities.

Table 2 End-to-end trajectory characteristics from initial conditions to science orbit insertion.

Characteristic	ESPA SmallSat	6U CubeSat
Time of Flight, Years	2.578	3.159
Total Maneuver Time, Years	0.997	1.297
Propellant Mass Used, kg	30.310	1.333

VII. Conclusions

A dynamical systems approach to trajectory design enables rapid and informed construction of an end-to-end trajectory for a small satellite to insert into an orbit around Sun-Earth L_5 from a fixed deployment condition near the Earth. Insight into natural flow mechanisms is used to formulate an itinerary that is discretized into multiple segments. Arcs within each of these segments are seeded from both natural dynamical structures generated in the Sun-Earth circular restricted three-body problem and low-thrust-enabled trajectories. Poincaré mapping is then used to rapidly analyze candidate arcs for their properties and their potential for connectivity to arcs in subsequent segments. Individual arcs that are selected within each segment are assembled to form an initial guess that is then input to a multiple shooting algorithm; the result is a nearby, continuous solution that is recovered in a point mass ephemeris model.

The presented approach is used to design low-thrust trajectories for a 180 kg SmallSat and a 6U CubeSat to each insert into bounded motions near Sun-Earth L_5 to perform targeted scientific observations for heliophysics. In this scenario, each of these spacecraft is assumed to ride as a secondary payload on a space telescope mission to a Sun-Earth L_2 quasi-halo orbit, supplying fixed deployment conditions near the Earth. The constructed trajectories for the SmallSat and CubeSat require, respectively, a flight time of 2.58 years and 3.16 years as well as a propellant mass that is 16.8% and 9.5% of the initial wet mass. These trajectories may be further refined in subsequent analyses to incorporate additional operational constraints or adjust the flight time and required propellant mass. However, the presented point solutions support two fundamental conclusions: the existence of low-thrust trajectories that may deliver a small satellite to the Sun-Earth L_5 region, subject to significant operational and propulsion constraints; and the capability to design these solutions rapidly, without a prohibitive analysis or computational burden. Given the limitations in trajectory design support for low-cost missions, this capability to recover a reasonable point design supports the potential for using small satellites to perform targeted scientific observations for heliophysics from locations well beyond low Earth orbit.

VIII. Acknowledgements

Part of this research was carried out at the Jet Propulsion Laboratory, California Institute of Technology, under a contract with the National Aeronautics and Space Administration and funded through the Internal Strategic University Research Partnerships (SURP) program. Part of this research was also performed at the University of Colorado Boulder. Government sponsorship acknowledged. The authors also appreciate valuable feedback from the reviewers.

References

[1] Akioka, M., Nagatsuma, T., Miyake, W., Ohtaka, K., and Marubashi, K., "The L5 Mission for Space Weather Forecasting," *Advances in Space Research*, Vol. 35, No. 1, 2005, pp. 65 – 69. doi:10.1016/j.asr.2004.09.014.

[2] Gibson, S. E., Vourlidas, A., Hassler, D. M., Rachmeler, L. A., Thompson, M. J., Newmark, J., Velli, M., Title, A., and McIntosh, S. W., "Solar Physics from Unconventional Viewpoints," *Frontiers in Astronomy and Space Sciences*, Vol. 5, 2018. doi:10.3389/fspas.2018.00032.

[3] Vourlidas, A., "Mission to the Sun-Earth L5 Lagrangian point: An Optimal Platform for Space Weather Research," *Space Weather*, Vol. 13, No. 4, 2015, pp. 197–201. doi:10.1002/2015SW001173.

[4] Kaiser, M., "The STEREO Mission: An Overview," *Advances in Space Research*, Vol. 36, No. 8, 2005, pp. 1483–1488. doi:10.1016/j.asr.2004.12.066.

[5] Kaiser, M., Kucera, T. A., Davila, J. M., Cyr, O. S., Guhathakurta, M., and Christian, E., "The STEREO Mission: An Introduction," *Space Science Review*, Vol. 136, 2008, pp. 5–16. doi:10.1007/s11214-007-9277-0.

[6] Webb, D. F., Biesecker, D. A., Gopalswamy, N., Cyr, O. C. S., Davila, J. M., Eyles, C. J., Thompson, B. J., Simunac, K. D. C., and Johnston, J., “Using STEREO-B as an L5 Space Weather Pathfinder Mission,” *Space Research Today*, Vol. 178, 2010, pp. 10–16. doi:10.1016/j.srt.2010.07.004.

[7] Freeman, A., “Exploring our Solar System With CubeSats and SmallSats: A NASA/JPL Perspective,” *The 4S Symposium*, 2018.

[8] Agasid, E., Burton, R., Carlino, R., Defouw, G., Perez, A. D., Karacalioglu, A. G., Klamm, B., Rademacher, A., Schalkwyk, J., Shimmin, R., Tilles, J., and Weston, S., “NASA State of the Art Report of Small Spacecraft Technology,” , 2019.

[9] Bosanac, N., Alibay, F., and Stuart, J. R., “A Low-Thrust Enabled SmallSat Heliophysics Mission to Sun-Earth L5,” *IEEE Aerospace Conference, Big Sky, MT*, 2018. doi:10.1109/AERO.2018.8396375.

[10] Spence, D., Ehrbar, E., Rosenbald, N., Demmons, N., Roy, T., Hoffman, S., Williams, W. D., Tsay, M., Zwahlen, J., Hohman, K., Hruby, V., and Tocci, C., “Electrospray Propulsion Systems for Small Satellites and Satlets,” *AIAA SPACE 2013 Conference and Exposition*, 2013. doi:10.2514/6.2013-5329.

[11] Lo, M., Llanos, P., and Hintz, G., “An L5 Mission to Observe the Sun and Space Weather, Part 1,” *AAS/AIAA Spaceflight Mechanics Meeting*, 2010. doi:10.13140/2.1.5166.0162.

[12] Llanos, P., Miller, J., and Hintz, G., “Mission and Navigation Design of Integrated Trajectories to L4,5 in the Sun-Earth System,” *AIAA/AAS Astrodynamics Specialist Conference*, 2012. doi:10.2514/6.2012-4668.

[13] Gopalswamy, N., Davila, J. M., Auchère, F., Schou, J., Korendyke, C. M., Shih, A., Johnston, J. C., MacDowall, R. J., Maksimovic, M., Sittler, E., Szabo, A., Wesenberg, R., Vennerstrom, S., and Heber, B., “Earth-Affecting Solar Causes Observatory (EASCO): a Mission at the Sun-Earth L5,” *Proceedings of SPIE - The International Society for Optical Engineering, Solar Physics and Space Weather Instrumentation IV*, Vol. 8148, 2011. doi:10.1117/12.901538.

[14] Fernandez, A., Heaton, A., and Heiligers, J., “Solar-Sail Transfers from Invariant Objects to L5 Periodic Orbits,” *7th International Conference on Astrodynamics Tools and Techniques (ICATT)*, 2018.

[15] Farres, A., Heiligers, J., and Miguel, N., “Road Map to L4/L5 with a Solar Sail,” *28th AIAA/AAS Space Flight Mechanics Meeting*, 2018. doi:10.2514/6.2018-0211.

[16] Sood, R., and Howell, K. C., “Solar Sail Transfers and Trajectory Design to Sun-Earth L4, L5: Solar Observations and Potential Earth Trojan Exploration,” *The Journal of the Astronautical Sciences*, Vol. 66, No. 3, 2019, pp. 247–281. doi:10.1007/s40295-018-00141-4.

[17] Koon, W. S., Lo, M. W., Marsden, J. E., and Ross, S. D., *Dynamical Systems, the Three Body Problem and Space Mission Design*, Marsden Books, 2011.

[18] Lo, M. W., “Libration Point Trajectory Design,” *Numerical Algorithms*, Vol. 14, 1997, pp. 153–164. doi:10.1023/A:1019108929089.

[19] Bosanac, N., "Leveraging Natural Dynamical Structures to Explore Multi-Body Systems," Ph.D. Thesis, Purdue University, West Lafayette, IN, 2016.

[20] Bosanac, N., Cox, A., Howell, K. C., and Folta, D. C., "Trajectory Design for a Cislunar CubeSat Leveraging Dynamical Systems Techniques: The Lunar IceCube Mission," *Acta Astronautica*, Vol. 144, 2018. doi:10.1016/j.actaastro.2017.12.025.

[21] Howell, K. C., Barden, B. T., Wilson, R. S., and Lo, M. W., "Trajectory Design Using a Dynamical Systems Approach With Application to Genesis," *AAS/AIAA Astrodynamics Specialist Conference*, 1997.

[22] Sullivan, C. J., Elliott, I., Bosanac, N., Alibay, F., and Stuart, J. R., "Exploring The Low-Thrust Trajectory Design Space for Smallsat Missions to the Sun-Earth Triangular Equilibrium Points," *29th AAS/AIAA Space Flight Mechanics Meeting*, 2019.

[23] Busek, "BHT-200 Busek Hall Effect Thruster," `http://www.busek.com/index_htm_files/70000700%20BHT-200%20Data%20Sheet%20Rev-.pdf`, Online; Accessed October 9th 2017.

[24] Accion Systems, "TILE - Tiled Ionic Liquid Electrospray," `http://www.accion-systems.com/tile`, Online; Accessed October 9th 2017.

[25] Pavlak, T. A., "Trajectory Design and Orbit Maintenance Strategies in Multi-Body Dynamical Regimes," Ph.D. Thesis, Purdue University, West Lafayette, IN, 2013.

[26] Szebehely, V., *Theory of Orbits: The Restricted Problem of Three Bodies*, London, UK: Academic Press, 1967.

[27] Folta, D. C., Bosanac, N., Guzzetti, D., and Howell, K. C., "An Earth–Moon System Trajectory Design Reference Catalog," *Acta Astronautica*, Vol. 110, 2015, pp. 341–353. doi:10.1016/j.actaastro.2014.07.037.

[28] Acton, C. H., "Ancillary Data Services of NASA's Navigation and Ancillary Information Facility," *Planetary and Space Science*, Vol. 44, 1996, pp. 65–70. doi:10.1016/0032-0633(95)00107-7.

[29] Irrgang, L., "Investigation of Transfer Trajectories to and from the Equilateral Libration Points L4 and L5 in the Earth-Moon System," Ph.D. Thesis, Purdue University, West Lafayette, IN, 2008.

[30] Vaquero, M., and Howell, K. C., "Leveraging Resonant-Orbit Manifolds to Design Transfers Between Libration-Point Orbits," *Journal of Guidance, Control and Dynamics*, Vol. 37, No. 4, 2014, pp. 1143–1157. doi:10.2514/1.62230.

[31] Haapala, A. F., "Trajectory Design in the Spatial Circular Restricted Three-Body Problem Exploiting Higher-Dimensional Poincare Maps," Ph.D. Thesis, Purdue University, West Lafayette, IN, 2014.

[32] Bosanac, N., Webster, C. M., Howell, K. C., and Folta, D. C., "Trajectory Design for the Wide Field Infrared Survey Telescope Mission," *Journal of Guidance, Control and Dynamics*, Vol. 42, No. 9, 2019, pp. 1899–1911. doi:10.2514/1.G004179.

[33] Grebow, D. J., "Generating Periodic Orbits In The Circular Restricted Three-Body Problem With Applications To Lunar South Pole Coverage," Master's Thesis, Purdue University, West Lafayette, IN, 2006.

[34] Pavlak, T. A., "Mission Design Applications in the Earth-Moon System: Transfer Trajectories and Stationkeeping," Master's Thesis, Purdue University, West Lafayette, IN, 2010.